

Inferring Turbulent Parameters via Machine Learning

Michele Buzzicotti¹, Fabio Bonaccorso¹, Luca Biferale¹

¹*Dept. Physics and INFN, University of Rome “Tor Vergata”, Italy.*

(Dated: January 4, 2022)

We design a machine learning technique to solve the general problem of inferring physical parameters from the observation of turbulent flows, a relevant exercise in many theoretical and applied fields, from engineering to earth observation and astrophysics. Our approach is to train the machine learning system to regress the rotation frequency of the flow’s reference frame, from the observation of the flow’s velocity amplitude on a 2d plane extracted from the 3d domain. The machine learning approach consists of a Deep Convolutional Neural Network (DCNN) of the same kind developed in computer vision. The training and validation datasets are produced by means of fully resolved direct numerical simulations. This study shows interesting results from two different points of view. From the machine learning point of view it shows the potential of DCNN, reaching good results on such a particularly complex problem that goes well outside the limits of human vision. Second, from the physics point of view, it provides an example on how machine learning can be exploited in data analysis to infer information that would be inaccessible otherwise. Indeed, by comparing DCNN with the other possible Bayesian approaches, we find that DCNN yields to a much higher inference accuracy in all the examined cases.

I. INTRODUCTION

Extracting information from the observation of a natural system is a fundamental problem in science. Except in the few cases where laboratory or numerical experiments are performed, inferring physical parameters is never easy [1, 2]. Measurements are always limited and our theoretical knowledge sometimes is inadequate to extract from them a correct description of the system. A significant example are turbulent flows [3–6]. Here because of chaos, any error in the observations increases exponentially in time, and quickly compromises our possibility to understand, predict, hence model turbulent behaviour. Consequences of such limitations are clear in fields like meteorology, oceanography and climate modeling [7–12]. In this work we aim to analyse turbulent flows in a different way. In particular, we use tools of Machine Learning (ML) developed in the field of computer vision such as Deep Convolutional Neural Network (DCNN) [13–16], to bring new perspectives in the data assimilation and analysis of complex physical systems [17–24]. The setup we consider is 3d turbulence under rotation [25]. There are multiple reasons for this choice, from the fundamental interest given by the high challenge to classify multiscale non-Gaussian fields to the specific relevance for geophysics and many applied flows realizations. Rotating turbulence is described by the Navier-Stokes equations (NSE) equipped with the Coriolis force,

$$\begin{cases} \partial_t \mathbf{u} + \mathbf{u} \cdot \nabla \mathbf{u} + 2\Omega \hat{z} \times \mathbf{u} = -\nabla p + \nu \Delta \mathbf{u} + \mathbf{f} \\ \nabla \cdot \mathbf{u} = 0, \end{cases} \quad (1)$$

here ν is the kinematic viscosity, $2\Omega \hat{z} \times \mathbf{u}$ is the Coriolis force produced by rotation, and Ω is the frequency of the angular velocity around the rotation axis \hat{z} . The fluid density is constant and absorbed into the definition of pressure p . \mathbf{f} , represents an external forcing mechanism. The relative importance of non-linear (advection) with respect to linear terms (viscous dissipation) is given by the Reynolds number, Re ,

$$Re = \frac{(\varepsilon_f^{1/3} k_f^{-4/3})}{\nu}, \quad (2)$$

where ε_f is the rate of energy input at the forcing scale $L_f \sim 1/k_f$. The larger is Re the more turbulence is developed in the dynamics. Rotation, at the same time, introduces a second non-dimensional control parameter in the equations, the Rossby number, Ro , which represents the ratio between rotation frequency and the flow characteristic time scale at the forcing wavenumber;

$$Ro = \frac{(\varepsilon_f k_f^2)^{1/3}}{\Omega}. \quad (3)$$

While it is well known that increasing Re leads the transition to turbulence, varying Ro leads to a second and more subtle transition. Indeed, in the limit of large Ro or small Ω , standard 3d homogeneous and isotropic turbulent dynamics is observed, on the other hand, increasing Ω , $Ro \leq 1$, the flow becomes almost bidimensional [26–30],

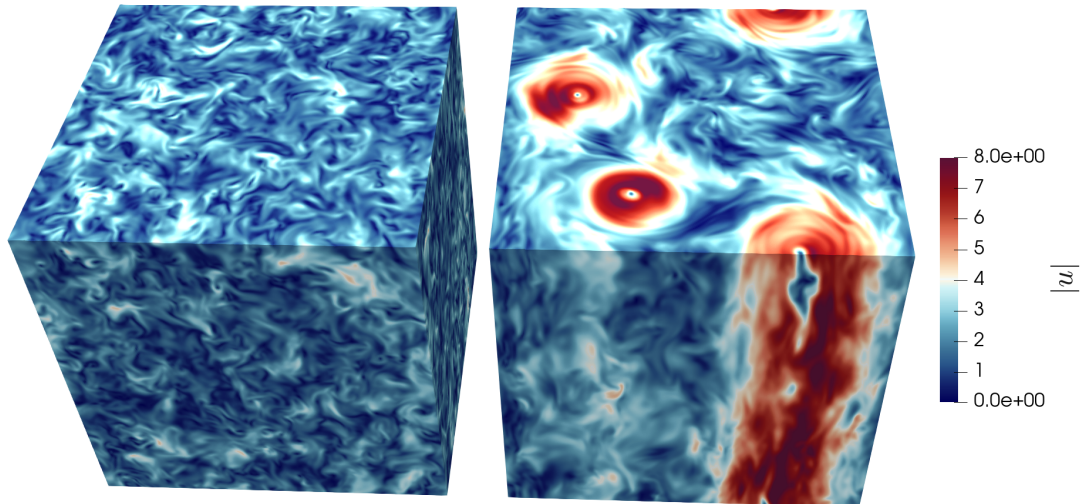


FIG. 1. 3D rendering of a turbulent flow under rotation at two different values of rotation rate, namely $\Omega = 4$ on the left side and $\Omega = 10$ in the right panel. In the first case the rotation frequency is small enough that the flow develops a dynamics similar to the standard 3D non-rotating case, with forward cascade of energy and small scales fluctuations. In the second case instead rotation is large enough to produce an inverse energy transfer that give rise to large-scales structures almost constant in the rotation direction.

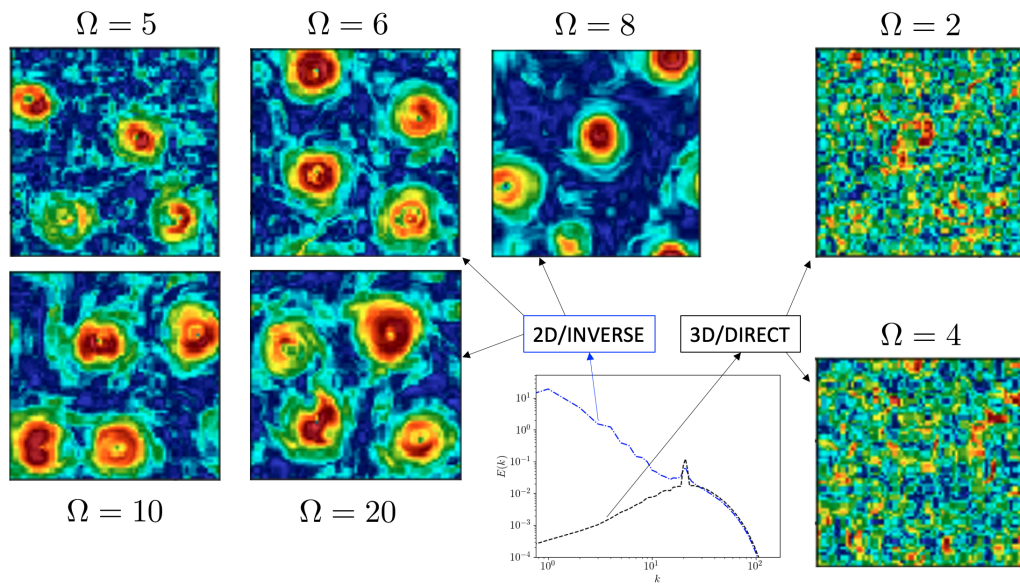


FIG. 2. Visualization of velocity magnitude on 2d planes extracted from a 3d domain, in the stationary regime for some of the different Ω values used in the regression problem. The fields at $\Omega \leq 4$ are in the direct cascade regime, while the higher rotation values the transition to split energy cascade regime is visible. The panel with the energy spectra, $E(k)$ vs k , shows an example of the energy distribution as a function of scale for the such systems at different values of Ω .

moving with constant velocity along the direction parallel to the rotation axis, i.e. \hat{z} . Simultaneously, at high rotation rates, the flow develops coherent/large-scales vortex like structures that live on the horizontal plane, (x, y) , as can be seen in the two renderings of Fig.1. These structures are fed by an inverse energy cascade that moves energy from where it is injected towards the larger scales available in the domain [31]. In other words, the transition induced by rotation consists in a change of the energy flux direction, from towards the small scales (direct cascade) to a split cascade regime with energy going simultaneously towards small and large scales [32, 33].

In Fig. 2 we present a visualization of the velocity module on planes extracted from 3d simulations varying the reference rotation rate Ω . As expected, for small values of Ω the flow is statistically isotropic and homogeneous, while increasing Ω large vortical structures appear in the dynamics. The nature of this transition, from direct to inverse cascade, is still not understood and also the transition threshold it is not known. Indeed, there are several reasons that complicate this problem, the high number of degrees of freedom and the length of the range of scales coupled in the dynamics are the main ones. An extra complication comes from the subtle way in which rotation affects the dynamics. To appreciate this point, one can notice that rotation produces the energy flux transition without doing any work on the system, $\langle \mathbf{u} \cdot (\hat{z} \times \mathbf{u}) \rangle = 0$. The result is that it is difficult to infer the Ω value from the analysis of the resulting flow field. For all these reasons this problem is a relevant example where measurements are not easily translated in information and new paradigm of analyses are needed. Some attempts in this direction have been followed in the recent years, using different tools like Fourier spatio-temporal decomposition [34] or nudging [35–37], however all these techniques require access to the temporal evolution to deduce the Ω value from the velocity field. In this work we aim to solve the same inverse problem of inferring Ω from the analysis of the velocity, using a DCNN designed and trained on this purpose. As discussed we expect to have only a partial knowledge of the system, and in particular we make the four following assumptions:

- Time evolution is not accessible
- Observations capture only a coarse-grained version of the velocity field
- We have access only to the velocity amplitude, $|\mathbf{u}|$
- We can observe the system on a 2d plane and not the full 3d domain

Each of these limitation strongly compromises our knowledge of the systems, however, as discussed above the first one is the most stringent. Indeed, up to our knowledge, there are not previous attempts based on Machine Learning techniques to attack the problem without any knowledge on the equations of motion. For comparison, in this work, we have repeated the same investigation using standard Bayesian Inference (BI) analysis. Results highlight the superiority of DCNN in solving regression problems and show how DCNN can be used to improve current data analysis capability. At the same time, in this work we tested DCNN on a much more challenging task than the standard image classification performed to simulate human vision [38–45]. We have also attempted to perform the same classification, using the unsupervised Gaussian Mixture Models (GMM) classification [46–48]. However we did not find any relation between the unsupervised classification and the rotation value, so it has not been included in the comparison with DCNN and BI. The paper is organized as follow. In Sect. II there is a detailed description of the datasets used in this work. In Sect. III we describe all methodologies, namely the DCNN and the BI. Results are presented in Sect. IV, and in Sect. V we draw our concluding remarks.

II. DATASET

A. Numerical Simulations

To generate the database of turbulent flows on a rotating reference frame, we have performed a set of Direct Numerical Simulations (DNS) of the NSE for incompressible fluid in a triply periodic domain of size $L = 2\pi$ with a resolution of $N = 256$ grid-points per spatial direction. We used a fully dealiased parallel 3d pseudospectral code, with time integration implemented as a second-order Adams-Bashforth scheme and the viscous term implicitly integrated. A linear friction term, $0.1\Delta^{-1}\mathbf{u}$, is added at wave-numbers with module $|\mathbf{k}| \leq 2$ to reach a stationary state. At the same time, viscous dissipation, $\nu\nabla^2\mathbf{u}$, is replaced by a hyperviscous term, $\nu\nabla^4\mathbf{u}$, with $\nu = 1.6 \times 10^{-6}$, to increase the inertial range of scales dominated by the non-linear energy transfer. The forcing mechanism, \mathbf{f} , is a Gaussian process delta-correlated in time, with support in wavenumber space around $k_f = 4$. The total energy time evolution for six simulations varying Ω is presented in Fig. 3(a), while in the panel (b) of the same figure we show the energy spectra, $E(k) = \frac{1}{2} \sum_{k \leq |\mathbf{k}| < k+1} |\hat{\mathbf{u}}(\mathbf{k})|^2$, averaged over time in the stationary regime for the same set of six simulations. From the energy spectra we can observe that while for $\Omega = 2$ (in the direct cascade regime) there is a depletion of energy at wavenumbers smaller than $|\mathbf{k}| < k_f$, for Ω values above the transition the split cascade regime, also the small wavenumbers are very energetic thanks to the inverse cascade suggesting the presence of large-scales structures in the flow.

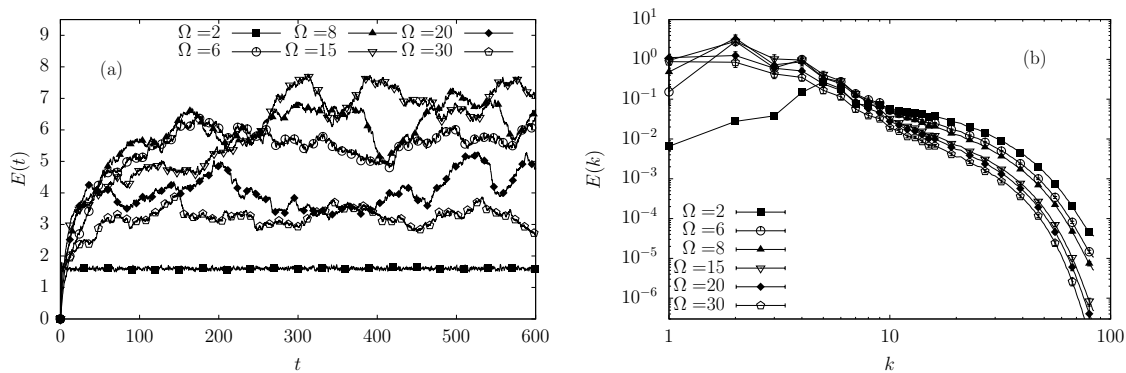


FIG. 3. (Panel a) Energy evolution of six different simulations performed with different Ω , from the direct to the inverse cascade regime. (Panel b) Energy spectra as a function of the wavenumbers for the same set of simulations. The spectra are averaged on time in the stationary regime, errorbars indicate the standard deviation and are generally inside the symbols size.

B. Dataset extraction

The ML training and validation datasets, accessible at the webpage <http://smart-turb.roma2.infn.it>, are extracted from the DNS described above, following [49], such as to match all assumption discussed in the introduction (Sect. I), namely;

- In order to vary the Rossby number, we performed ten numerical simulations each with a different rotation frequency. Two simulations well below the transition in the direct cascade regime, $\Omega = 2, 4$, three of them in the transition region, $\Omega = 5, 6, 7$, and the remaining five well inside the split cascade regime with $\Omega = 8, 10, 15, 20, 30$.
- For each of the ten simulations we have dumped a number of roughly 600 snapshots of the full 3d velocity field with a temporal separation large enough to decrease correlations between two successive data-points (see Fig. 3(a) for the total energy evolution).
- Each snapshot at the original resolution of 256^3 grid points is downsized on a coarser grid of 64^3 grid-points, after applying a Galerkin truncation in Fourier space where the maximum frequency is set to $|\mathbf{k}| \leq 32$.
- For each downsized configuration, 16 horizontal planes (x, y) , (perpendicular to the rotation axis), are selected at different z and for each of them we computed the module of the velocity field as; $|\mathbf{u}| = \sqrt{u_x^2 + u_y^2 + u_z^2}$.
- To increase the dataset, we shift each of the 16 planes in 11 different ways, by choosing randomly a new center of the plane and using periodic boundary conditions, such as to obtain a total number of 176 planes at each instant of time and a total of $600 \times 176 = 105600$ planes for each Ω value.

The full dataset, in this way, is composed of more than 1 million different velocity module planes, out of which the 80% of them are used as training set while 20% are used as validation set. To be sure that validation data were never seen during training, none of the planes used in the validation set is obtained from a random shift of a plane contained in the training set. Instead, the two sets are built using the same protocol but from different temporal realization of the flow splitting its time evolution in two separate parts.

III. METHODS

A. Deep Convolutional Neural Network (DCNN)

Fig. 4 schematizes the ML problem set-up. A plane of velocity module randomly extracted from the dataset of ten simulations is given in input to a DCNN with the goal to infer the Ω value of the simulation from which the plane has been extracted. The training is performed in a supervised setting, having pre-labelled all planes with their corresponding value, Ω_{true} . As solution of the regression problem, the DCNN gives in output a real number corresponding to the predicted rotation value, Ω_{pred} . In this way the inferring task is not limited to a predefined set

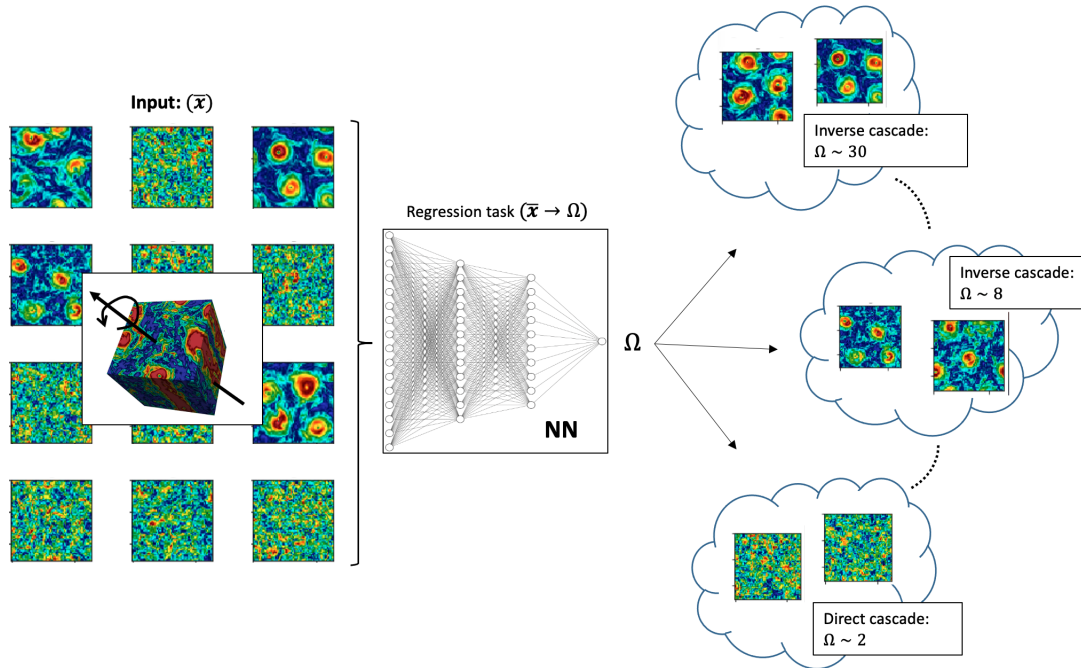


FIG. 4. Visual representation of the DCNN input-output setup used in the regression problem. The neural network is trained to map a plane of velocity module extracted from 3d data to the rotation frequency of the reference frame.

of classes and can be generalized to estimate rotation values never observed during training. The network is trained to *minimize* the following loss function;

$$\mathcal{L} = \mathbb{E}\{(\Omega_{true} - \Omega_{pred})^2\}, \quad (4)$$

which is the mean-squared-error between the target value Ω_{true} and the predicted value Ω_{pred} . \mathbb{E} is the mean over a mini-batch of 256 different planes. To implement the DCNN we used TensorFlow [50] libraries with a Python interface, optimized to run on GPUs. As described in Fig. 5 the overall architecture is composed of three convolutional layers that encode the input plane of velocity module on 64 different planes of size 16×16 . This first part of the network is the one asked to identify all the relevant features of the velocity planes relevant to the regression problem. The data/features are then reshaped into a single vector of 512 elements. The second half of the network, is composed by two fully connected layers that transform the 512-dimensional vector into the real number representing the network prediction, Ω_{pred} . The training of these two final fully connected layers is performed using a dropout of 60% to reduce overfitting issues [51]. All layers are followed by a non-linear ReLu activation functions. In the main panel of Fig. 6 we show the evolution of the loss, \mathcal{L} , measured on the training and validation data as a function of the number of epochs. From their evolution we see that there is no evidence of overfitting with the two losses remaining always of the same order. We considered training converged after roughly 250 epochs where the cost of the validation set starts to saturate. Using a mini-batch of 256 planes, and a training dataset of $N_{tra} = 844800$ planes, each epoch consists of 3300 back-propagation steps. The backpropagation has been performed with an Adam optimizer equipped with a Nesterov momentum [52] using a learning rate of 10^{-5} . To achieve a good training with the learning protocol just introduced, we have normalized the input data to be in the $[0; 1]$ range, namely we rescaled the module intensity of each grid-point by normalizing it by the maximum value calculated over the whole training set. The same normalization constant has been used to rescale the validation set. In the same way the training labels Ω_{true} have been rescaled by their maximum value in the training. In the inset of Fig. 6, we show the Probability Density Function (PDF) of predicting the correct rotation value using the DCNN on the validation set at different epochs during training. Here $\Omega_{true} = 20$ is used, but similar behaviours are observed for all the other Ω . At epoch 350 the PDF becomes close to a delta-like distribution, suggesting very good accuracy of the network, with errors only every few cases over one-thousand, and always within 20% the correct value.

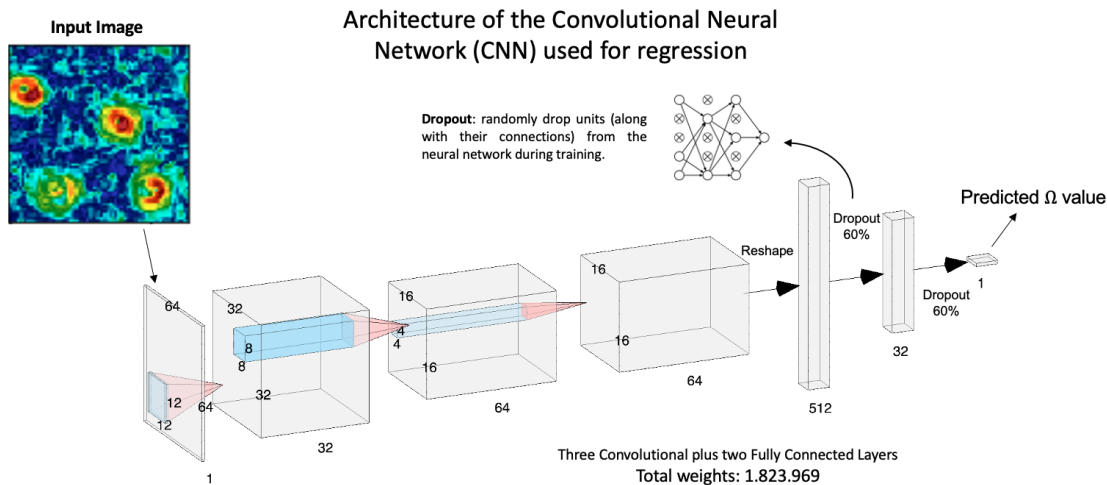


FIG. 5. Details of the Deep Convolutional Neural Network implemented in the regression problem. The network is composed of three first convolutional layers that map the input plane to 64 different 16x16 images, that after a reshape are mapped to the rotation prediction, Ω , by two fully connected layers. All layers are followed by a ReLu activation function, a dropout of 60% follows the last two fully connected layers.

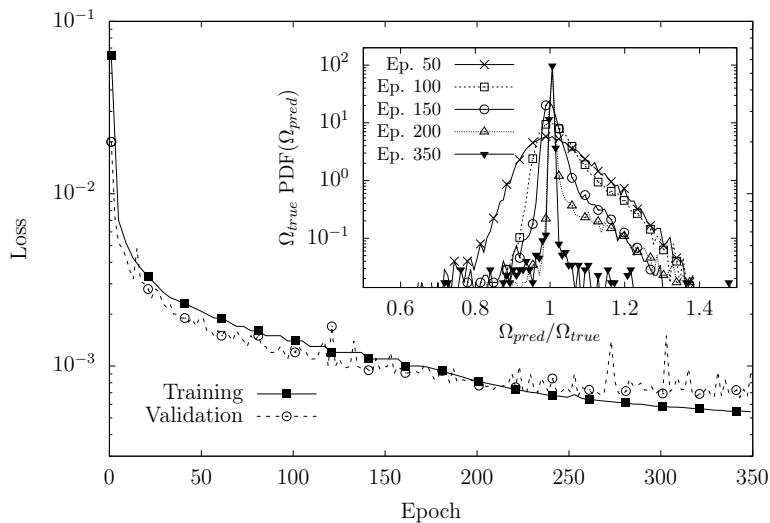


FIG. 6. (Main panel) Evolution of the Loss during the different training epochs, measured on the training set (solid line full squares) and on the validation set (dashed line open circles). (Inset) Probability Density Function (PDF), measured at different epochs, of the predicted rotation frequency, Ω_{pred} , normalized to the real value used in the simulation, $\Omega_{true} = 20$. The PDF is measured on the validation set.

B. Bayesian Inference

The second statistical inference approach considered in this work is based on the Bayes' Theorem [53–55]. The idea is to infer properties of the flow assuming the knowledge of some underlying probability distributions. More specifically, the theorem tells us that the posterior probability, $P(\Omega_i|\mathcal{O})$, of observing Ω_i given a measure of another generic observable, \mathcal{O} , can be estimated as follow;

$$P(\Omega_i|\mathcal{O}) = \frac{P(\mathcal{O}|\Omega_i)P(\Omega_i)}{P(\mathcal{O})} = \frac{P(\mathcal{O}|\Omega_i)P(\Omega_i)}{\sum_i P(\mathcal{O}|\Omega_i)P(\Omega_i)}. \quad (5)$$

$P(\Omega_i)$ is the prior probability, in our case for all Ω_i equal to 0.1 because the dataset is composed by the same number of planes for each of the ten Ω_i . $P(\mathcal{O}|\Omega_i)$, instead, is the likelihood to get the measure \mathcal{O} of a generic observable for

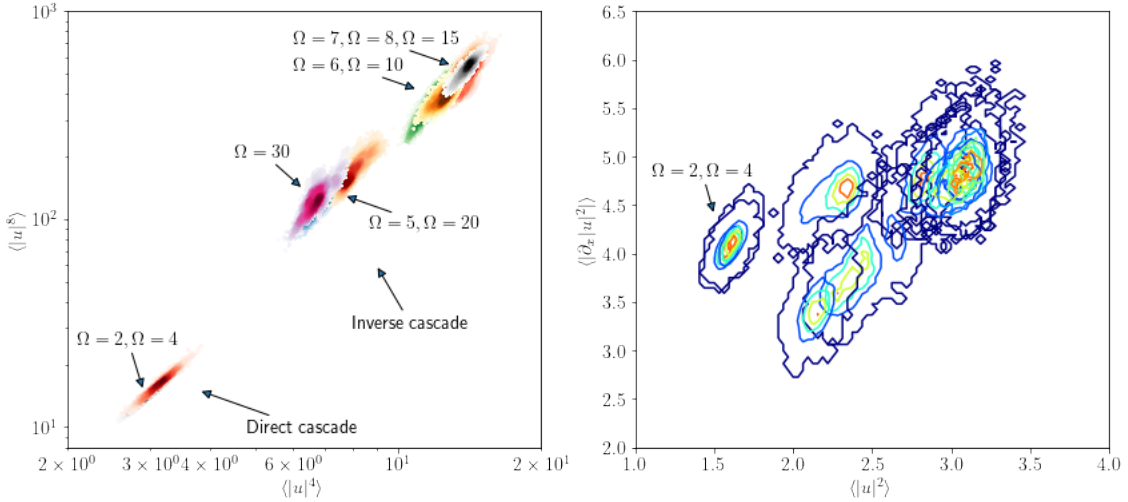


FIG. 7. (Left panel) Scatterplot in log-log scale of the fourth and eighth order moments of the mean velocity module, averaged the 2d different planes. (Right panel) Joint-likelihood, $P(\langle u^2 \rangle, \langle (\partial_x u)^2 \rangle | \Omega_i)$, of the squared velocity module and its derivative along the x direction, measured for the ten different Ω . The joint-PDF is measured from the training set of planes, and colours from dark-blue to red are proportional to the PDF value. The first cluster on the left consists of planes in the direct cascade, as indicate by the labels, the other clusters are composed by the overlapping of the remaining Ω values.

a fixed Ω_i . Once known the posterior probability in Eq. (5), a first Bayes estimation can be obtained as follows;

$$\bar{\Omega}_{Bay} = \sum_{i=1}^{10} P(\Omega_i | \mathcal{O}) \Omega_i, \quad (6)$$

which correspond to the mean value on the posterior probability. A second possible estimation can be done as the most likely Ω_i given \mathcal{O} , namely;

$$\Omega_{Bay}^* = \max_{\Omega_i} P(\Omega_i | \mathcal{O}) = \max_{\Omega_i} P(\mathcal{O} | \Omega_i) P(\Omega_i), \quad (7)$$

where in the last step the denominator of (5) is neglected because it does not affect the maximization on Ω_i . For our specific set-up we have chosen two different observables that could be relevant for the inference of the correct Ω and at the same time accessible from the analysis of the dataset. The first is the mean energy, $\langle u^2 \rangle$, and the second is the mean squared gradient, $\langle (\partial_x u)^2 \rangle$, where $u = |\mathbf{u}|$, and the angular brackets, $\langle \dots \rangle$, are the average over the plane surface. For each of these observables we have calculated the likelihood $P(\mathcal{O} | \Omega_i)$ from the 80 thousand planes for each Ω_i of the training dataset. Namely we have measured; $P(\langle u^2 \rangle | \Omega_i)$, $P(\langle (\partial_x u)^2 \rangle | \Omega_i)$ and the joint-likelihood, $P(\langle u^2 \rangle, \langle (\partial_x u)^2 \rangle | \Omega_i)$ on the training set. At this point, measuring the same observables on the validation dataset, and knowing the likelihoods for each Ω_i , we could estimate the posterior probability $P(\Omega_i | \mathcal{O})$ (Eq. (5)) and than infer $\Omega_{Bay}(\mathcal{O})$ (Eq. (6)), on the validation planes. Before moving to the results, to highlight the difficulties of such problem in the left panel of Fig. 7 we show a scatterplot of the fourth vs the eight order moments of the velocity module for each of the 20 thousand planes of the validation set. Different colours indicate different rotation values as indicated by the arrows and labels, while the intensity of the colours is proportional to the density of points accumulated in that region. From the scatterplot we can differentiate three main clusters, the first is composed by the planes in the direct cascade regime, while the other two are made of planes from simulations around or above the transition. Inside these three main clusters it is not possible to distinguish any specific Ω_i . Furthermore, moments amplitude is not a monotonic function of the Ω_i . The right panel of Fig. 7 shows the joint-likelihood of the two observables introduce above, mean energy and mean gradients. From this plot we can see that measuring gradients does not allow to have a better statistical separation of the different Ω and only the points below-above the transition are always possible to be inferred. In the next section we present and discuss results of Ω inference via DCNN and standard Bayesian approach.

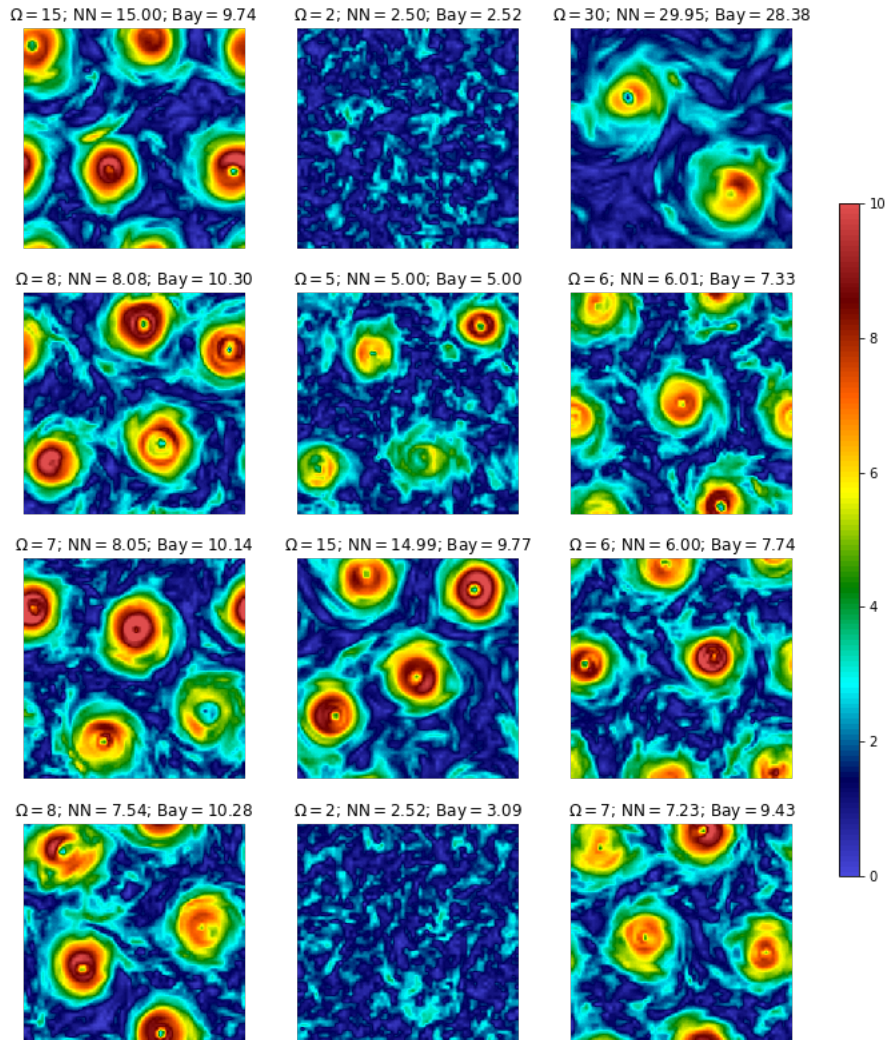


FIG. 8. Visualization of few examples of velocity planes extracted from the validation set. Each plane reports in the title its reference rotation rate, (Ω), sided respectively by the neural network (NN) and the Bayes (Bay) predictions.

IV. RESULTS

As already pointed out, guessing the correct Ω value from the observation of the velocity planes is a challenge much beyond human vision capability. To appreciate it, in Fig. 8 we present a random selection of 12 planes extracted from our validation dataset. Above each panel we have reported the exact Ω value of the simulation, and the corresponding prediction obtained by the DCNN analysis and the Bayes inference, using the joint-likelihood $P(\langle u^2 \rangle, \langle (\partial_x u)^2 \rangle | \Omega_i)$. These first results are already suggesting that the DCNN prediction is closer to the correct Ω than the Bayes one. In particular, the network's uncertainties, (the neural network outputs a real number and not a class), are generally small enough to allow the correct classification on the corresponding Ω , on the contrary the Bayes inference leads to a miss-classification of the rotation parameter. A quantitative comparison of the two techniques is presented in Fig. 9, where in the four panels we report a scatterplot between the correct rotation value, Ω_{true} and the corresponding prediction obtained via the DCNN (top left panel), and the Bayes inference with the three different likelihoods, namely the one based on the mean energy (top right panel), on the mean square gradients (bottom left panel) and on the joint likelihood combining energy and gradients (bottom right panel). The four panels are all obtained with the same validation dataset of roughly 20 thousands planes for each of the ten Ω values. The symbols size and color intensity are proportional to the density of points in the specific region of the scatterplot, while the open hexagon in black represents the mean value measure over all planes for each Ω . The DCNN estimates are the more accurate both in terms of its mean and variance, being most of the time close to the identity (dotted) line indicating the

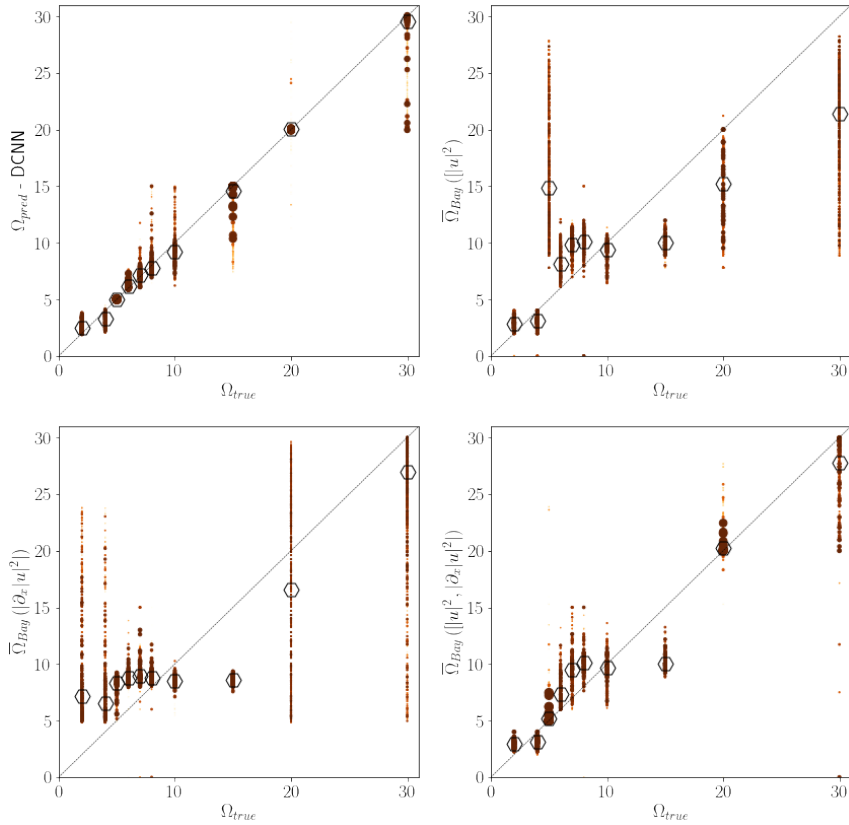


FIG. 9. Scatterplot of inferred vs the real rotation value. Where the inference is obtained with the DCNN, Ω_{pred} (top-left panel), or with Bayes, $\bar{\Omega}_{Bay}$, conditioning on the PDF of the velocity square module (top-right panel), on the gradients of the velocity square module (bottom-left panel) or with the joint PDF of velocity module and its gradients (bottom-right panel). The dashed line indicate the identity function, while the red dots are the predictions for each planes on the validation set, the mean values predicted for each Ω_{true} are reported in black lines and the errorbars represent the standard deviation over all estimations.

perfect correspondence between Ω_{true} and Ω_{pred} . From Fig. 9 we can conclude that Bayesian inference based on the knowledge of likelihood on the mean energy allows only to classify among below and above transition values (top-right panel), while the same analysis repeated on the mean squared gradients likelihood, is not even enough to classify such transition. This can be explained by the fact that mean energy is a larger scale observable than the mean squared gradients, hence it is able to better highlight the formation of the large-scales vortexes. On the other hand, combining the two information at large and small scales the joint-likelihood Bayes estimate improve its prediction quality and even if it does not allow to distinguish close Ω values such as in the range $5 \leq \Omega \leq 15$ at least it allows to always classify values below the transition $\Omega \leq 4$, close to the transition $5 \leq \Omega \leq 15$ and large rotation far from the transition $\Omega \geq 20$. The more detailed comparison is presented in Fig. 10, where in ten different panels we report the PDF of the DCNN and Bayes predictions, for all Ω over all planes of validation set. Each PDF is normalized to corresponding rotation value such as $\Omega_{pred}/\Omega_{true} = 1$ indicates the correct prediction. The Bayes inference reported in this figure is based on the knowledge of the joint-likelihood $P(\langle u^2 \rangle, \langle (\partial_x u)^2 \rangle | \Omega_i)$, which as already found gives a higher accuracy. The PDFs for the predictions in the direct cascade regime ($\Omega = 2 \& 4$) show difficulties for both approaches to distinguish the two cases. This is not surprising, indeed, before the transition no large-scale coherent structures are expected to appear in the flow and the resulting field should be almost equivalent for all rotation rates and similar to the non-rotating homogeneous and isotropic case. At the same time comparing the two PDFs before the transition we notice that while Bayes peaks always at the center between the two values, the DCNN is correctly peaked around one in both cases, suggesting that rotation is affecting the flow since before the inverse energy transfer is established in the dynamics. For all the other Ω after the transition, and in particular at intermediate rotation rate, the DCNN accuracy is always better than classical Bayesian approach. The final comparison is presented in Fig.11 which contains a summary of what already shown by previous the PDFs. Here, indeed, it is shown the mean difference between the predicted and the true Ω value for all the different classes considered. The average also in this case is measured over all the estimations for all validation planes of each of the ten classes, and the error are

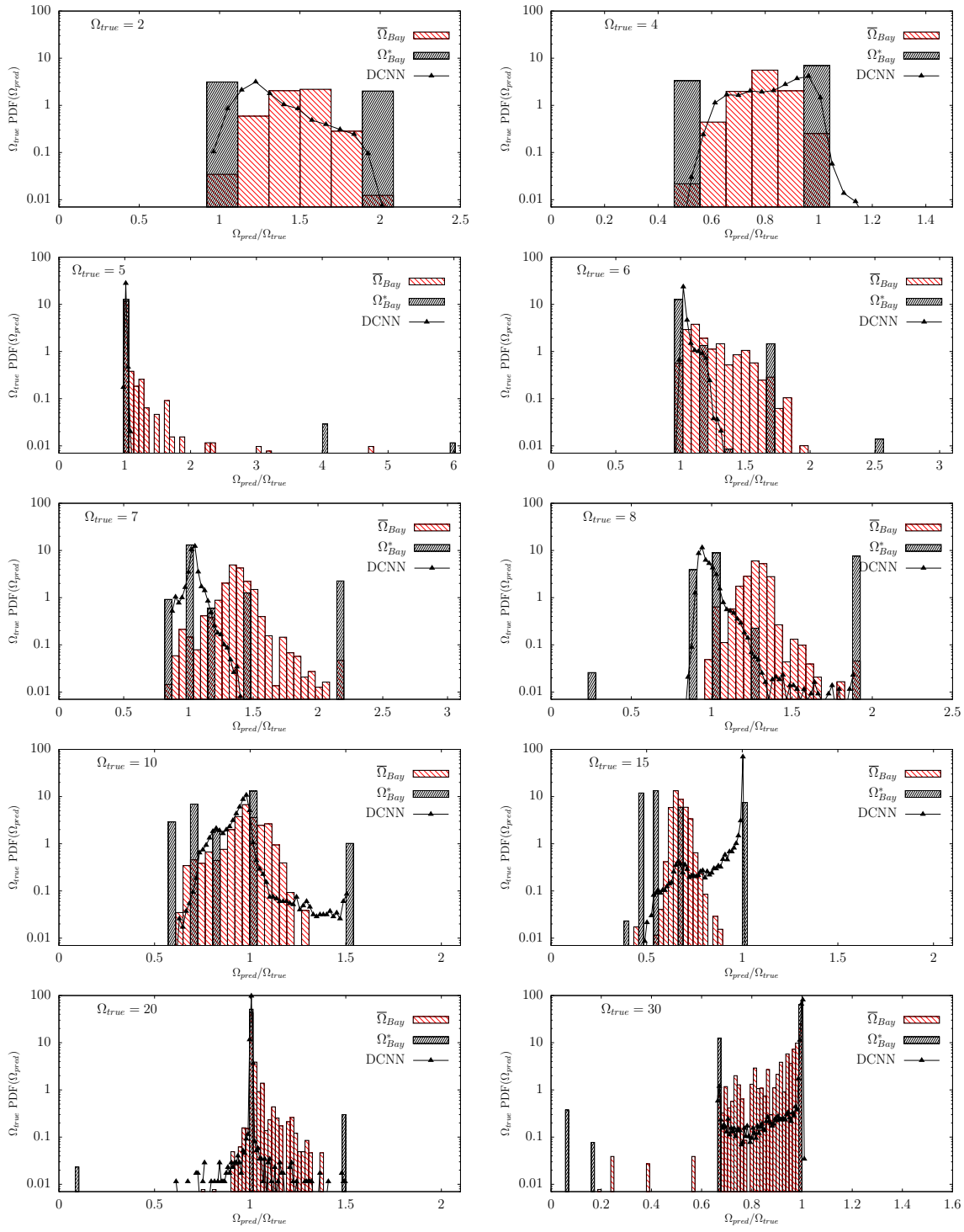


FIG. 10. PDF of rotation value predicted by the neural network, Ω_{pred} (DCNN, solid lines full triangles), compared with the mean, $\bar{\Omega}_{Bay}$ (black histograms), and most likely, Ω_{Bay}^* (red histograms), Bayes estimations using joint-likelihood $P(\langle u^2 \rangle, \langle (\partial_x u)^2 \rangle | \Omega_i)$, on the validation set. For the sake of data presentation each of the PDF measured on the ten different Ω values are reported in different panels. As indicated in the axis, the PDF are all normalized by their corresponding Ω_{true} indicate in the labels of each panel.

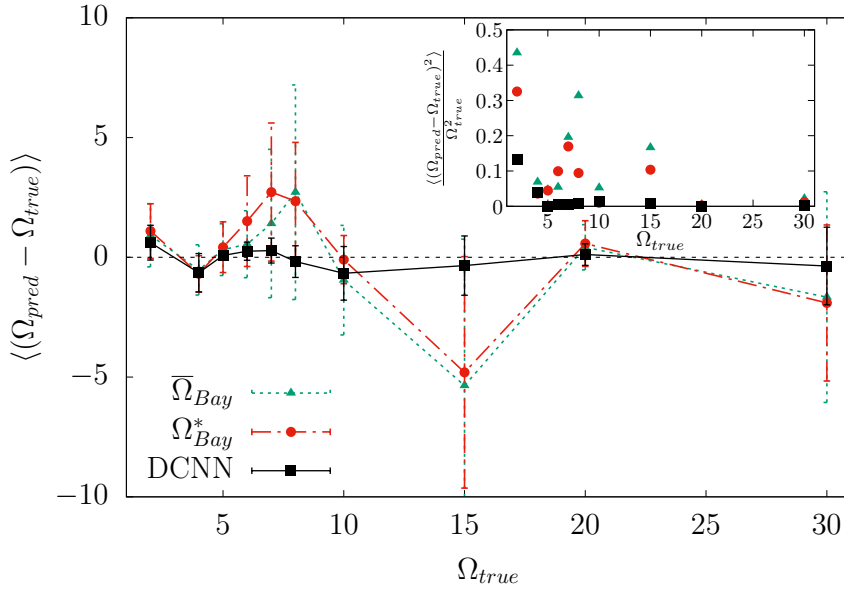


FIG. 11. (Main panel) Mean deviation between the predicted and true value of Ω for each of the ten classes considered, the errorbars show the root mean square of the difference between Ω_{pred} and Ω_{true} . (Inset) Mean squared difference between prediction and true Ω normalized to the square of the correct rotation value for each of the ten classes. The average is taken over the validation dataset, while the predictions are obtained as in Fig. 10, by the neural network, DCNN, or as the mean, $\bar{\Omega}_{Bay}$ and most likely, Ω_{Bay}^* (red histograms), Bayes estimations using joint-likelihood $P(\langle u^2 \rangle, \langle (\partial_x u)^2 \rangle | \Omega_i)$.

estimated as the root mean square of the same quantity. In this figure we can see, as observed before, that the mean value of the DCNN prediction is for all Ω closer to the true value, indeed the black squared dots are always closer to zero than the other cases reporting the Bayes inference. At the same time also the standard deviation around the mean is always smaller for the DCNN case than for the other Bayesian results. This final observation allows us to conclude that the classification produced by the neural network is in all terms more efficient the one achieved with the Bayesian approach.

V. CONCLUSIONS

We have implemented a Deep Convolutional Neural Network (DCNN) inspired by the computer vision community to analyze data of turbulent flows under rotation with the goal to infer the rotation frequency of the reference frame from the resulting flow velocity field. To put our self in a realistic scenario we assumed to have just a limited knowledge of the flow, and in particular we imagined to have access only to a bidimensional cut of the full 3d domain and to have the velocity only at a fixed time during the evolution. As argued, these two assumptions make the problem difficult enough that no other tools of analysis are known to be able to achieve such goal under the same conditions, and allowed us to show how Machine Learning can push forward our data analysis capability. Indeed, results showed that even a simple DCNN properly trained has been able to solve such problem with unprecedented accuracy. For comparison, the only other possible way to repeat the same inference without using temporal information, was to use a standard Bayesian inference based on different observables. For us, the natural choice from the type of problem and the available data, was to measure moments of the velocity field and of the velocity gradients. As discussed all results have highlighted the potential of DCNN, that were able to outperform any other inference attempt. As briefly discussed in the introduction, an unsupervised classification of the same dataset has been attempted using a GMM classification algorithm, however no relation between the classes identified and the rotation value has been found. Indeed GMM, as more in general k-means algorithms [56], are mainly sensitive to the number of vortexes inside each plane and to their spatial location, hence, to observables that are not closely connected to the rotation value but can only be used to distinguish the dynamics above and below the transition threshold from direct to inverse cascade. For this reason a detailed analysis using this tool has been omitted in the paper. From this study we want to bring two main messages. The first is, from a physics point of view, that Machine Learning provides tools that can be highly beneficial in problems of data analysis of complex systems, the work presented in [24] is another example. Second, on the other hand, is to show how physical systems can be ideal testing grounds for new ML algorithms,

where they can be evaluated objectively and compared quantitatively on much more challenging tasks than the ones of general objects recognition or classification. It is far from us to think that ML can always offer best solutions to data analysis, but instead we aim to bring an example of how ML and physics can benefit from each other, hoping that this work will lead to further and deeper investigations in such direction.

ACKNOWLEDGEMENT

The authors thank Prof. Roberto Benzi for many useful discussions. This work was supported by the European Research Council (ERC) under the European Union’s Horizon 2020 research and innovation programme (Grant Agreement No. 882340), and by the project Beyond Borders (CUP): E84I19002270005 funded by the University of Rome Tor Vergata.

-
- [1] Steven L Brunton, Joshua L Proctor, and J Nathan Kutz, “Discovering governing equations from data by sparse identification of nonlinear dynamical systems,” *Proceedings of the national academy of sciences* **113**, 3932–3937 (2016).
 - [2] Marc Bocquet, Julien Brajard, Alberto Carrassi, and Laurent Bertino, “Data assimilation as a learning tool to infer ordinary differential equation representations of dynamical models,” *Nonlinear Processes in Geophysics* **26**, 143–162 (2019).
 - [3] Uriel Frisch, *Turbulence: the legacy of AN Kolmogorov* (Cambridge University Press, 1995).
 - [4] Stephen B. Pope, *Turbulent Flows* (Cambridge University Press, 2000).
 - [5] Peter A Davidson, Yukio Kaneda, Keith Moffatt, and Katepalli R Sreenivasan, *A voyage through turbulence* (Cambridge University Press, 2011).
 - [6] Karthik Duraisamy, Gianluca Iaccarino, and Heng Xiao, “Turbulence modeling in the age of data,” *Annual Review of Fluid Mechanics* **51**, 357–377 (2019).
 - [7] Geoffrey K Vallis, *Atmospheric and oceanic fluid dynamics* (Cambridge University Press, 2017).
 - [8] Joseph Pedlosky *et al.*, *Geophysical fluid dynamics*, Vol. 710 (Springer, 1987).
 - [9] Ian F Akyildiz, Weilian Su, Yogesh Sankarasubramaniam, and Erdal Cayirci, “Wireless sensor networks: a survey,” *Computer networks* **38**, 393–422 (2002).
 - [10] Eugenia Kalnay, *Atmospheric modeling, data assimilation and predictability* (Cambridge university press, 2003).
 - [11] Michele Buzzicotti, Benjamin A Storer, Stephen M Griffies, and Hussein Aluie, “A coarse-grained decomposition of surface geostrophic kinetic energy in the global ocean,” *Earth and Space Science Open Archive* , 58 (2021).
 - [12] Alberto Carrassi, Michael Ghil, Anna Trevisan, and Francesco Uboldi, “Data assimilation as a nonlinear dynamical systems problem: Stability and convergence of the prediction-assimilation system,” *Chaos: An Interdisciplinary Journal of Nonlinear Science* **18**, 023112 (2008).
 - [13] Alex Krizhevsky, Ilya Sutskever, and Geoffrey E Hinton, “Imagenet classification with deep convolutional neural networks,” *Advances in neural information processing systems* **25**, 1097–1105 (2012).
 - [14] Kaiming He, Xiangyu Zhang, Shaoqing Ren, and Jian Sun, “Deep residual learning for image recognition,” in *Proceedings of the IEEE conference on computer vision and pattern recognition* (2016) pp. 770–778.
 - [15] Olaf Ronneberger, Philipp Fischer, and Thomas Brox, “U-net: Convolutional networks for biomedical image segmentation,” in *International Conference on Medical image computing and computer-assisted intervention* (Springer, 2015) pp. 234–241.
 - [16] Joseph Redmon, Santosh Divvala, Ross Girshick, and Ali Farhadi, “You only look once: Unified, real-time object detection,” in *Proceedings of the IEEE conference on computer vision and pattern recognition* (2016) pp. 779–788.
 - [17] Ian Goodfellow, Yoshua Bengio, and Aaron Courville, *Deep learning* (MIT press, 2016).
 - [18] Steven L Brunton and J Nathan Kutz, *Data-driven science and engineering: Machine learning, dynamical systems, and control* (Cambridge University Press, 2019).
 - [19] Steven L Brunton, Bernd R Noack, and Petros Koumoutsakos, “Machine learning for fluid mechanics,” *Annual Review of Fluid Mechanics* **52**, 477–508 (2020).
 - [20] Luca Biferale, Fabio Bonaccorso, Michele Buzzicotti, Patricio Clark Di Leoni, and Kristian Gustavsson, “Zermelo’s problem: Optimal point-to-point navigation in 2d turbulent flows using reinforcement learning,” *Chaos: An Interdisciplinary Journal of Nonlinear Science* **29**, 103138 (2019).
 - [21] Michele Buzzicotti, Fabio Bonaccorso, P Clark Di Leoni, and Luca Biferale, “Reconstruction of turbulent data with deep generative models for semantic inpainting from turb-rot database,” *Physical Review Fluids* **6**, 050503 (2021).
 - [22] Julien Brajard, Alberto Carrassi, Marc Bocquet, and Laurent Bertino, “Combining data assimilation and machine learning to emulate a dynamical model from sparse and noisy observations: a case study with the lorenz 96 model,” *Geoscientific Model Development Discussions* , 1–21 (2019).
 - [23] Francesco Borra and Marco Baldovin, “Using machine-learning modeling to understand macroscopic dynamics in a system of coupled maps,” *Chaos: An Interdisciplinary Journal of Nonlinear Science* **31**, 023102 (2021).
 - [24] Alessandro Corbetta, Vlado Menkovski, Roberto Benzi, and Federico Toschi, “Deep learning velocity signals allow quantifying turbulence intensity,” *Science Advances* **7**, eaba7281 (2021).

- [25] Alexandros Alexakis and Luca Biferale, “Cascades and transitions in turbulent flows,” *Physics Reports* **767**, 1–101 (2018).
- [26] Enrico Deusebio, Guido Boffetta, Erik Lindborg, and Stefano Musacchio, “Dimensional transition in rotating turbulence,” *Physical Review E* **90**, 023005 (2014).
- [27] Raffaele Marino, Pablo Daniel Mininni, Duane Rosenberg, and Annick Pouquet, “Inverse cascades in rotating stratified turbulence: fast growth of large scales,” *EPL (Europhysics Letters)* **102**, 44006 (2013).
- [28] Raffaele Marino, Pablo Daniel Mininni, Duane L Rosenberg, and Annick Pouquet, “Large-scale anisotropy in stably stratified rotating flows,” *Physical Review E* **90**, 023018 (2014).
- [29] Michele Buzzicotti, Hussein Aluie, Luca Biferale, and Moritz Linkmann, “Energy transfer in turbulence under rotation,” *Physical Review Fluids* **3**, 034802 (2018).
- [30] P Clark Di Leoni, Alexandros Alexakis, L Biferale, and M Buzzicotti, “Phase transitions and flux-loop metastable states in rotating turbulence,” *Physical Review Fluids* **5**, 104603 (2020).
- [31] Leslie M Smith and Fabian Waleffe, “Transfer of energy to two-dimensional large scales in forced, rotating three-dimensional turbulence,” *Physics of fluids* **11**, 1608–1622 (1999).
- [32] Kannabiran Seshasayanan and Alexandros Alexakis, “Condensates in rotating turbulent flows,” *Journal of Fluid Mechanics* **841**, 434–462 (2018).
- [33] Adrian van Kan and Alexandros Alexakis, “Critical transition in fast-rotating turbulence within highly elongated domains,” *Journal of Fluid Mechanics* **899** (2020).
- [34] P Clark di Leoni, Pablo J Cobelli, and Pablo D Mininni, “The spatio-temporal spectrum of turbulent flows,” *The European Physical Journal E* **38**, 1–10 (2015).
- [35] Patricio Clark Di Leoni, Andrea Mazzino, and Luca Biferale, “Inferring flow parameters and turbulent configuration with physics-informed data assimilation and spectral nudging,” *Physical Review Fluids* **3**, 104604 (2018).
- [36] Patricio Clark Di Leoni, Andrea Mazzino, and Luca Biferale, “Synchronization to big data: Nudging the navier-stokes equations for data assimilation of turbulent flows,” *Physical Review X* **10**, 011023 (2020).
- [37] Michele Buzzicotti and Patricio Clark Di Leoni, “Synchronizing subgrid scale models of turbulence to data,” *Physics of Fluids* **32**, 125116 (2020).
- [38] Joel Janai, Fatma Güney, Aseem Behl, Andreas Geiger, *et al.*, “Computer vision for autonomous vehicles: Problems, datasets and state of the art,” *Foundations and Trends® in Computer Graphics and Vision* **12**, 1–308 (2020).
- [39] Haggai Maron, Or Litany, Gal Chechik, and Ethan Fetaya, “On learning sets of symmetric elements,” in *International Conference on Machine Learning* (PMLR, 2020) pp. 6734–6744.
- [40] Stanislav Pidhorskyi, Ranya Almohsen, Donald A Adjeroh, and Gianfranco Doretto, “Generative probabilistic novelty detection with adversarial autoencoders,” arXiv preprint arXiv:1807.02588 (2018).
- [41] Mingxing Tan, Ruoming Pang, and Quoc V Le, “Efficientdet: Scalable and efficient object detection,” in *Proceedings of the IEEE/CVF conference on computer vision and pattern recognition* (2020) pp. 10781–10790.
- [42] Siddharth Singh Chouhan, Uday Pratap Singh, and Sanjeev Jain, “Applications of computer vision in plant pathology: a survey,” *Archives of computational methods in engineering* **27**, 611–632 (2020).
- [43] Wen-Huang Cheng, Sijie Song, Chieh-Yun Chen, Shintami Chusnul Hidayati, and Jiaying Liu, “Fashion meets computer vision: A survey,” *ACM Computing Surveys (CSUR)* **54**, 1–41 (2021).
- [44] Xin Feng, Youni Jiang, Xuejiao Yang, Ming Du, and Xin Li, “Computer vision algorithms and hardware implementations: A survey,” *Integration* **69**, 309–320 (2019).
- [45] Deepak Pathak, Philipp Krahenbuhl, Jeff Donahue, Trevor Darrell, and Alexei A Efros, “Context encoders: Feature learning by inpainting,” *Proceedings of the IEEE conference on computer vision and pattern recognition*, , 2536–2544 (2016).
- [46] Carl Edward Rasmussen *et al.*, “The infinite gaussian mixture model.” in *NIPS*, Vol. 12 (Citeseer, 1999) pp. 554–560.
- [47] Douglas A Reynolds, “Gaussian mixture models.” *Encyclopedia of biometrics* **741**, 659–663 (2009).
- [48] Xiaofei He, Deng Cai, Yuanlong Shao, Hujun Bao, and Jiawei Han, “Laplacian regularized gaussian mixture model for data clustering,” *IEEE Transactions on Knowledge and Data Engineering* **23**, 1406–1418 (2011).
- [49] Luca Biferale, Fabio Bonaccorso, Michele Buzzicotti, and Patricio Clark di Leoni, “TURB-Rot. A large database of 3d and 2d snapshots from turbulent rotating flows. <http://smart-turb.roma2.infn.it>,” arXiv:2006.07469 (2020).
- [50] Martín Abadi, Paul Barham, Jianmin Chen, Zhifeng Chen, Andy Davis, Jeffrey Dean, Matthieu Devin, Sanjay Ghemawat, Geoffrey Irving, Michael Isard, *et al.*, “Tensorflow: A system for large-scale machine learning,” in *12th {USENIX} symposium on operating systems design and implementation ({OSDI} 16)* (2016) pp. 265–283.
- [51] Nitish Srivastava, Geoffrey Hinton, Alex Krizhevsky, Ilya Sutskever, and Ruslan Salakhutdinov, “Dropout: a simple way to prevent neural networks from overfitting,” *The journal of machine learning research* **15**, 1929–1958 (2014).
- [52] Timothy Dozat, “Incorporating nesterov momentum into adam,” (2016).
- [53] Richard C Aster, Brian Borchers, and Clifford H Thurber, *Parameter estimation and inverse problems* (Elsevier, 2018).
- [54] Bradley Efron, “A 250-year argument: Belief, behavior, and the bootstrap,” *Bulletin of the American Mathematical Society* **50**, 129–146 (2013).
- [55] David JC MacKay, “Bayesian interpolation,” *Neural computation* **4**, 415–447 (1992).
- [56] Daniel D Lee and H Sebastian Seung, “Learning the parts of objects by non-negative matrix factorization,” *Nature* **401**, 788–791 (1999).